Research Square

Preprints are preliminary reports that have not undergone peer review.
They should not be considered conclusive, used to inform clinical practice,
or referenced by the media as validated information.

Investigations of structural, optical and electrical conductivity of Zn1+xMnxFe2-2xO4 ferrite nanoparticles

Abdul Hakim .Ahmed . Al Hammadi
Sana'a University
Fatima .Ahmad . Abu Holikah
f.abuholikah@su.edu.ye

Sana'a University
Fatima. Mohammed . Thabit
Sana'a University

Article

Keywords: Spinel ferrite nanomaterial's, Doping with zinc (Zn2+) and manganese (Mn4+) ions- X-ray diffraction, Optical properties by FTIR and UV-Vis analysis, Alternating current electrical conductivity (σac)

Posted Date: May 22nd, 2026

DOI: https://doi.org/10.21203/rs.3.rs-9545690/v1

License: This work is licensed under a Creative Commons Attribution 4.0 International License.
Read Full License

Additional Declarations: No competing interests reported.

Investigations of structural, optical and electrical conductivity of $Zn_{1+x}Mn_xFe_{2-2x}O_4$ ferrite nanoparticles

Abdul Hakim .Ahmed . Al Hammadi [1], Fatima .Ahmad. Abu Holikah [1,2]✉*, Fatima. Mohammed . Thabit [1]

[1]*Department of Physics, Faculty of Sciences, Sana'a University, Sana'a , Yemen .*

[2]*Department of Physics, Faculty of Education, Applied Sciences and Humanities Khawlan, Sana'a University, Sana'a, Yemen*

✉* *Corresponding author . email: f.abuholikah@su.edu.ye*

Abstract

Spinel ferrite nanoparticles $Zn_{1+x}Mn_xFe_{2-2x}O_4$, where X = (0.0, 0.1, 0.2, 0.3, 0.4, 0.5), Spinel nanoparticles with zinc (Zn^{2+}) and manganese (Mn^{4+}) ions, were synthesized using the sol-gel method with citric acid. A comprehensive analysis was performed using X-ray diffraction (XRD), Fourier transform infrared (FTIR) spectroscopy, UV-Vis spectroscopy, and electrical conductivity. The results showed that the samples possess a single-phase cubic spindle crystal structure. The electrical conductivity (σac) was also investigated as a function of frequency. The formation of ZMF nanoparticles was confirmed by FTIR and UV-Vis analysis of the samples. The nanoparticles exhibited energy gaps in the semiconductor region. UV-Vis analysis revealed gaps in the optical energy band, which increased with increasing zinc and manganese concentrations. FTIR spectra showed major absorption bands, confirming the formation of a spinel ferrite phase. AC conductivity was observed as a function of both temperature and frequency, with experimental results showing that the AC conductivity (σac) increased with increasing frequency. Electrical conductivity also increased with increasing temperature, indicating the semiconducting nature of the compound. The average crystal size ranged from 36.84 to 37.57 nm. The results demonstrate that the studied material is a promising alternative material for a wide range of applications due to its unique properties. The energy gap of the nanocomposites was determined using UV-Vis spectroscopy, with results of 2.631 to 2.389 eV, respectively, indicating improved conductivity. These results showed that the $Zn_{1+x}Mn_xFe_{2-2x}O_4$ compound has high capacity and high loss as well, making it a promising choice for advanced electronic devices such as computer memory cards, microwave absorbers, and capacitors.

Keywords: *Spinel ferrite nanomaterial's - Doping $Zn_{1+x}Mn_xFe_{2-2x}O_4$ with zinc (Zn^{2+}) and manganese (Mn^{4+}) ions- X-ray diffraction - Optical properties by FTIR and UV-Vis analysis - Alternating current electrical conductivity (σ_{ac}).*

Introduction

In recent times, researchers and students have shown increasing interest in spinel ferrite materials (AF2O4, where A is Co, Ni, Mn, Zn, Mg) due to their distinctive insulating, magnetic, and optical properties. These materials are characterized by their ease of fabrication and environmental stability. The physical and chemical properties of these materials also influence the properties of the ferrite. which depends on numerous aspects involving preparation conditions such as grinding time, sintering temperature and heating and cooling rate [1-2]. The sol–gel have been used to create MFe_2O_4 nanoparticles [3]. The most alluring techniques is co-precipitation because of its easy experimental setup and ultrafine particles with high yield at low sintering temperatures [4] . It is essential to get the high-density powder with small and homogenous grain size, it can be achieved using wet chemical synthesis techniques, such as the sol–gel method, which offers a wide range of advantages over other techniques [5-6-7]. Ferrite has widely employed in various applications such as magnetic sensors, data storage devices, actuators, audio recordings, and biotechnology Ferrites can thus be utilized as computer memory cores and antenna cores, inductors, switching devices, transformers, microwave latching mechanisms, and so on .Nowadays, the ferrites are extensively employed in the commercial field because of their superior magnetic and electrical characteristics [8,9,10,11]. Information storage, magnetic resonance imaging, ceramic coatings for solar cells, optoelectronic devices, and electronic devices [12-13]. The optical properties of the dielectric materials generally became of interest because of their sensible transmission within the optical part of the spectrum as compared with different categories of materials. So that in order to study the optical properties of the ferrite materials, the optical constants such as absorption coefficient, transmission, reflection, and index of refraction are vital parameters to explain the optical properties of the ferrite materials. [14.15] The Zn-Mn ferrites was different by substituting Zn^{2+} ions, which prefer tetrahedral sites, with divalent metal ions that either adopt octahedral positions or inhibit grain growth and the magnetic properties tailored with careful addition [16, 17,18, 19].. The octahedral sites are occupied by Mn^{4+} and Fe^{3+}, whereas the tetrahedral sites are occupied by Zn^{2+} and Fe^{3+}. explain the optical properties of the ferrite materials. within the zinc-substituted Ba (Co1xZnx)2Fe16O27 [17] Rani *et al.* reported a decrease in the saturation magnetization when increasing the zinc concentration for the cobalt zinc ferrites composition synthesis by the ceramic method[18] The general behavior for the nickel ferrites prefers to occupy the octahedral sites while the zinc prefers to occupy the tetrahedral site. The

interactions between the tetrahedral ions and octahedral sites will alter the electrical and magnetic properties of ferrites. The octahedral sites are occupied by Ni^{2+} and Fe^{3+}, whereas the tetrahedral sites are occupied by Zn^{2+} and Fe^{3+}. The properties of the ferrite are also strongly dependent on the synthesis method, sintering temperature, chemical composition, etc.[19.20.21] The knowledge of types of band gap energy, direct or indirect structure, is very important for deciding what material can be used in a device requiring light output. The electrical conductivity (σ_{ac}) was studied as a function of frequency (from 100 kHz to 1 kHz) within a temperature range of 304 to 461.4 K. Energy gaps were observed at different zinc and manganese concentrations, with the nanoparticles exhibiting energy gaps in the semiconductor region. The alternating current (AC) conductivity was observed as a dependence of both temperature and frequency, with experimental results showing that the AC conductivity (σ_{ac}) increased with increasing frequency. The electrical conductivity also increased with increasing temperature, indicating the semiconducting nature of the compound . Fe^{2+} ions occupying octahedral positions are formed. This leads to increased electron exchange between Fe^{2+} and Fe^{3+}, polarization, and improved conductivity. These results revealed that $Zn_{1+x}Mn_xFe_{2-2x}O_4$ has high capacitance and high loss, making it a promising choice for electronic equipment such as computer memory cards, microwave absorbers, and capacitors.

Experimental procedure

Materials. The sol–gel method [22_23] was used to prepare $Zn_{1+x}Mn_xFe_{2-2x}O_4$ nanoparticles, which includes the following steps. Metal ions [$Mn(NO_3)_4.8H_2O$], [$Zn(NO_3)_2.6H_2O$], and [$Fe(NO_3)_3.9H_2O$] were used as starting materials with a purity of 99% (MI), along with Ethylenediaminetetraacetic acid and citric acid in a molar ratio.

$$Metal\ Nitrates\left|(1+x)Zn^{2+}+xMn^{4+}+(2-2x)Fe^{3+}+citric\ acid\right|$$
$$\xrightarrow{800C^{\circ}\ sol-gel\ comoustoin} Zn_{1+x}\ Mn_x\ Fe_{2-x}\ O_4$$
$$+Gases\uparrow(Co_2, N, H_2o)$$

The resulting compound is $Zn_{1+x}Mn_xFe_{2-2x}O_4$.

Experimental setup

The candidate samples $Zn_{1+x}Mn_xFe_{2-2x}O_4$ where x = (0.0, 0.1, 0.2, 0.3, 0.4, and 0.5) were prepared using the gel solution auto-combustion manufacturing methods. Metal ions [$Mn(NO_3)_4.8H_2O$], [$Zn(NO_3)_2.6H_2O$], and [$Fe(NO_3)_3.9H_2O$] were used as starting materials with a purity of 99% (MI), along with ethylenediaminetetraacetic- acid (E.D.T.A) and citric - acid (C.A) in a molar ratio. For each sample, 40 g of E.D.T.A and 40 g of C.A were mixed in a flask, with 60 ml of distilled water. The mixture was then stirred for 6hours at room temperature. The mixture solutions were placed in electric stove. Ammonium hydroxide was then used, and the mixture was stirred for another 6hours at 60C(until homogeneity was achieved and a gel formed. To dry the samples, they were placed in an oven at 120 C(overnight. Finally, the beaker was placed on an electric stove where the temperature was increased to the 350C(, for 30 seconds. The samples were sintered at 880C(, for 4hours,.

Instrumentation:

The optical properties of the samples were investigated using a UV-Vis spectrometer, using U-3900-Japan , located at the same position as the photovoltaic cells, measure the intensity of the emitted light. The meter records and displays the values on an LCD screen. Electronic detectors were also used to measure and compare the intensity of the light beams. X-ray diffraction (XRD) were also used to measure the structural properties with a geotechnical survey using CuKα radiation (λ = 0.154C^o) were collected (VISXD-2 X-ray diffraction China) . Infrared spectra of all samples in this series were recorded at room temperature in the range of 400 cm^{-1} to 4000 cm^{-1} using a Fourier transform spectrometer , at room temperature (using a Perkin-Elmer spectrometer (model 783) with potassium bromide as the solvent). The electrical conductivity of all samples were investigated . Using the– lock-in amplifier SR510 Stamford Research Systems .

Results and discussion

X-ray diffraction analysis.

The X-ray diffraction pattern of the $Zn_{1+x}Mn_xFe_{2-2x}O_4$ nanoparticles composite shows in fig 1. This figure shows only one phase of spinel ferrite. The samples were also found to be concordant, which was confirmed by the structure of $Zn_{1+x}Mn_xFe_{2-2x}O_4$ nanoparticles, spinel ferrite at Fd-3m . All reflection lines for the ferrite samples agree well with the standard powder diffraction data from JCPDS.1012-22. [27] No other lines were observed, indicating that the samples contain only one phase, face center cubic and that there are no signs of other phases or residues in the samples. Furthermore, it was observed that each peak shifted towards a lower 2θ value with the substitution of Mn^{4+} and Zn^{2+} ions in the $Zn_{1+x}Mn_xFe_{2-2x}O_4$ lattice. The average crystalline domain size (D) can be calculated from the well-known Scherrer's equation. [24] , [25] where λ is the X-ray wavelength, K is a constant frequently referred to the crystallite-shape factor. A value of 0.9 is used assuming spherical crystallites with cubic unit cells β_{hkl} . [26]

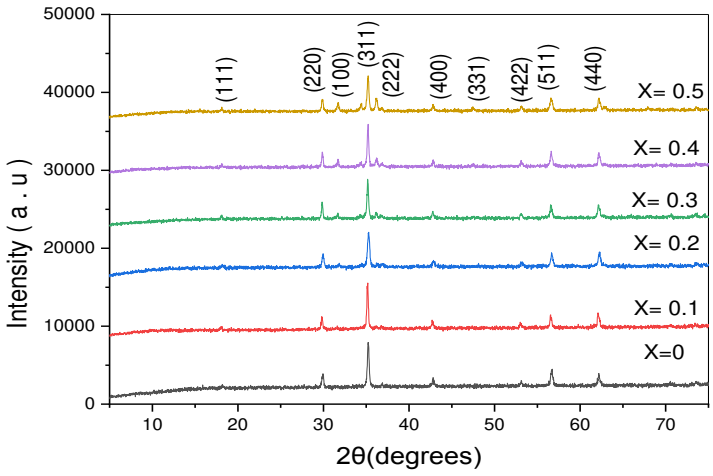


Figure 1. x-ray diffraction patterns for $Zn_{1+x}Mn_xFe_{2-2x}O_4$

The slight shift of the peaks indicates an zigzag in both the crystal size and the lattice parameters, respectively.

The characteristic diffraction peaks of these phases were precisely identified, with no peaks associated with secondary phases, impurities, or hydroxides in the sample. The crystalline nature of the sample was

assessed based on the sharp and strong x-ray diffraction peaks, and in accordance with standard [27] . The cell size (v), lattice constant (a), the distance between crystal planes [28,29-30] (ρ_x) XRD density, and apparent density (ρ_b) and Grain size (nm) were calculated. All them are listed in Table 1. The Shearer equation was used to calculate the grain size (D) [31] for $Zn_{1+x}Mn_xFe_{2-2x}O_4$ nanoparticles. The dislocation density was also calculated [32,33-34]

X	a (nm)	ρ_x gm/cm^3	ρ_b gm/cm^3	V (nm^3)	grain size (nm)
0	0.843	5.29721	5.17667	0.59907711	37.5702
0.1	0.846	5.25438	5.19042	0.60549574	40.30895
0.2	0.843	5.31472	5.17508	0.59907711	33.97959
0.3	0.844	5.29039	5.19461	0.60121158	42.49303
0.4	0.852	5.28039	5.10858	0.61847021	41.48395
0.5	0.845	5.28848	5.01099	0.60335112	36.83904

Table 1. x-ray density(ρ_x),, bulk density (ρ_b), lattice constant (a),volume (v), grain size.(D) . $Zn_{1+x}Mn_xFe_{2-2x}O_4$ Nano composites

The x-ray density (ρ_x) was calculated by using equation

$$\rho_x = \frac{Z\ M}{N_A\ V_{cell}}$$

where, M is the molecular mass of sample, Z=8 is the number of molecules per unit cell, N_A is Avogadro's number. and V_{cell} is the volume of the unit cell . The calculated values of x-ray density ρ_x are listed in table 1. The x-ray density value , looks like zigzag . This behavior depends on the molecular weight, the close packing of the plane of the unit cell of the sample and the migration of Mn^{+4} and Mn^{+2} in the unit cell.

Bulk density (ρ_b) was estimated by using the following equation .

$$\rho_b = \frac{M}{V_{sample}}$$

where M is the mass of the sample , V= (r^2 h), where h is the thickness, and r is the radius. The values of bulk density are just less than x-ray density.

Optical measurements.

Infrared (IR) analysis.

Fig 2., shows the plots of infrared spectra of $Zn_{1+x}Mn_xFe_{2-2x}O_4$ (x = 0.0, 0.1, 0.2, 0.3, 0.4 and 0.5) Nano-ferrite. The spectra were recorded at room temperature in the frequencies range of 400–4000 cm $^{-1}$. Tow frequencies band confirmed the higher frequency band ν_1- (571–599 cm^{-1}) and lower frequency band ν_2 (434-464 cm^{-1}) are assigned, the tetrahedral and octahedral sites, respectively .[35- 36] Thus, the formation of a single-phase cubic structure of Nano-ferrites was confirmed to clear the cubic structure with the formation of two kinds of characteristic absorption bands found at around 434-460 cm^{-1} and 571-599 cm^{-1}. These were associated with the stretching vibrations of tetrahedral (A-site) and octahedral (B-site) sites, respectively [37] . The IR spectra exhibits also tow frequencies band in the wavenumber range above 1000cm^{-1} , the absorption bands found at 1634.33cm^{-1} and 3426.87cm^{-1}. Absorption bands in the range of 400–1000 cm^{-1} are related to metal-oxygen bonds, such as Mn-O (Mn^{+4} ,Mn^{+6}) vibrations and O – H (H_2O, ..) vibrations. The band positions and number of absorption peaks are dependent on the crystalline structure, chemical composition, and particle morphology .[38]

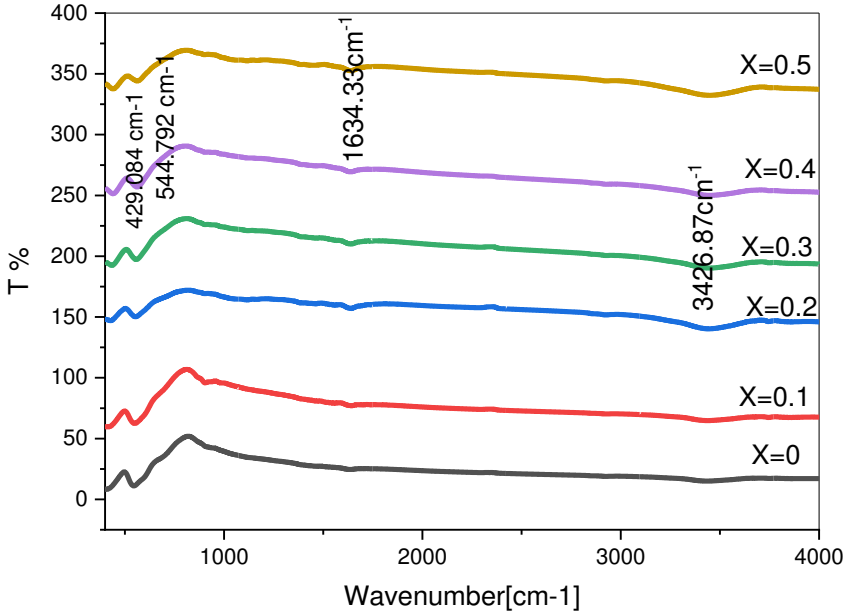


Figure 2. Shows that FT-IR spectra for $Zn_{1+x}Mn_xFe_{2-2x}O_4$ (x= 0.0, 0.1, 0.2, 0.3, 0.4 and 0.5).

Composition	Absorption band	Absorption band	Force constants	Force constants	Bond Lengths	Bond Lengths
X	$\nu_2\,(cm^{-1})$	$\nu_1\,(cm^{-1})$	Dyne/cm^2	Dyne/cm^2	(B-O)	(A-O)
			$K_{oct}\times10^5$	$K_{tct}\times10^5$	B-O	A-O
X=0	429.084	544.792	2.18049832	3.12907669	2.23037	1.8546
X=0.1	410.763	548.649	2.00537935	2.87777601	2.23831	1.8612
X=0.2	429.084	553.471	2.18049832	3.12907669	2.23037	1.8546
X=0.3	432.941	557.327	2.22250844	3.18936214	2.23301	1.8568
X=0.4	439.691	562.148	2.31406904	3.32075445	2.25418	1.8744
X=0.5	440.655	562.148	2.30514185	3.30794367	2.23566	1.8591

Table 2 . IR bands, force constants (K_{oct} and K_{tet}), bond lengths (vibration B-O and vibration A-O), as a function of X - concentrations .

It can be observed from the IR plots that the band positions and changes slightly. This may be due to the distribution of Mn and Zn ions (ionic radius 0.64 Å) which are replacing Fe^{3+} ions (ionic radius of 0.67 Å) at the octahedral [B] site; thus, making some changes in the size of the tetra- and octahedral-sites. It can be seen that the wave number frequency shifted to higher frequencies with increasing Mn and Zn content, and the values of frequency bands are shown in figure 2. The fluctuation in the cations-oxygen bond length of the spinel's octahedral lattice may be the cause of the shift in band locations that occurs when the Mn content is increased. The displacement of Fe^{3+} ions by smaller Mn ions, will result in a somewhat decrease in the metal-oxygen bond length and consequently will increase the wave number of bands. The band vibration in the range 1550 -1634.33 cm^{-1} may be logically attributed to the increasing quantity of the $Mn^{4+} - O^{2-}$ complexes as the Fe^{3+} content decreases at the B-site. The broad absorption in the 3350–3650 cm^{-1} range is attributed to the – OH groups of H_2O, indicating the existence of water absorbed on the surface of ZnO nanograins.[39]

The table 2. Shows the variation of the force constant K_{oct} and K_{tet} which may be as a result of variation of the cations oxygen bond length.

The hopping length L is the distance between the ions in the

tetrahedral and octahedral given as . $L_A = a\sqrt{3}/4$, $L_B = a\sqrt{2}/4$ where, a is the lattice parameter. The Waldron's force constant **K_{oct} and K_{tet}** given as.

$$K_{oct} = 10.62(M_B/2)\nu_2^2 \times 10^{-3} \quad , \quad K_{tet} = 7.62(M_A)\nu_1^2 \times 10^{-3}$$

Where ν_1 *and* ν_2 *are bonds vibrations in* cm^{-1} , M_A *and* M_B are the molecular mass of cations distribution for the composations[39,,40]

UV–Vis spectroscopy.

Absorption coefficient (α).

The optical properties of the Mn-Zn, nanoparticles samples are studied by UV–visible spectra. The transmission spectra of all the synthesized materials showed almost an opposite behavior to that seen in Fig. 3. Obviously, the optical transmission increased in the visible region for all the synthesized materials and possesses maximum value for Zn^{2+} Mn^{4+} $Fe^{3+}O4$. The absorption coefficient (α) value can be computed via the following equation:

$$\alpha = 2.303A / t \ .^{40}$$

The change in α (λ) for $Zn_{1+x}Mn_xFe_{2-2x}O_4$ is presented in Fig. 3. From this Figure ,it can be seen that α decreases as the wavelength (λ) of the incident photon increases. The extinction coefficient (α) value can be calculated via the following equation :

$$k = 4\lambda \ ^{41,42}$$

The absorption coefficient (α)[43] was calculated as α = 2.303 A/t, where t is the sample thickness and A is the absorbance. The highest absorption coefficient is shown in two locations .

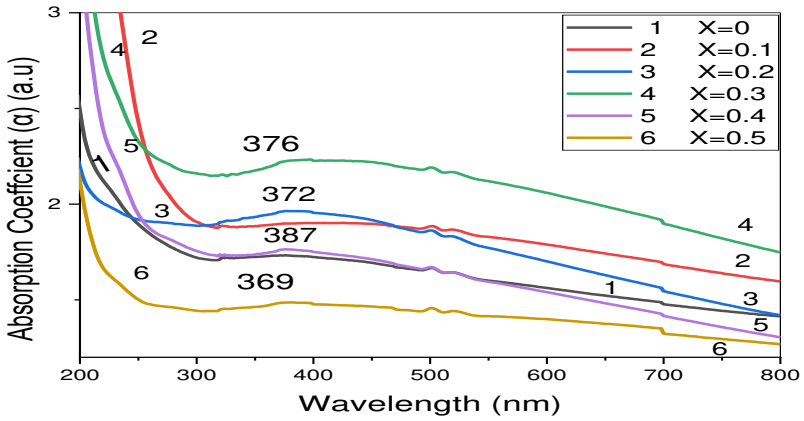


Figure 3. Absorption spectra of $Zn_{1+x}Mn_xFe_{2-2x}O_4$ (X = 0.0, 0.1, 0.2, 0.3, 0.4, 0.5) Nano composites .

The first is in the violet region at (Δ = 334 nm), where the absorption is 30%. Direct electron transitions are expected at these wavelengths (high photon energy). The second was performed in the ultraviolet region , where the absorption is 70%. The figure shows that the absorption coefficient decreases with increasing incident wavelength for all ferrite samples up to a specific wavelength that varies depending on the ferrite sample. At the wavelength surrounding 300nm, α becomes nearly plenty broad band. The absorption coefficient values in the ultraviolet region decrease sharply with decreasing wavelength. This is attributed to the absorption properties of this samples.

Extinction coefficient (K) and refractive index (n).

Extinction coefficient (k) versus wavelength of $Zn_{1+x}Mn_xFe_{2-2x}O_4$ (x= 0.0,0.1,0.2,0.3,0.4 and 0.5) Nano composites is presented in Fig. 4. It can be observed that k increases as the wavelength of the incident photon increases

The extinction coefficient is a unique property of a material's composition, indicating its ability to absorb light of a specific wavelength. It is calculated as the fraction of light lost due to scattering and absorption per unit average distance. The extinction coefficient (k),

which can be calculated using Equation [44] is a measure of the fraction of light lost due to scattering and absorption per unit distance.

$$\mathbf{K = \alpha\lambda/4\pi}$$ [44]

In Figure 4 , it is shown that the extinction coefficient of the sample behaves similarly to the absorption coefficient as a function of wavelength. The extinction coefficient decreases with increasing wavelength. The value of the extinction coefficient decreases with increasing zinc content. The extension coefficient indicates the proportion of light lost at this location due to scattering and absorption. Furthermore, the curved nature of the (k) and the curved absorption coefficient are shown to be identical.

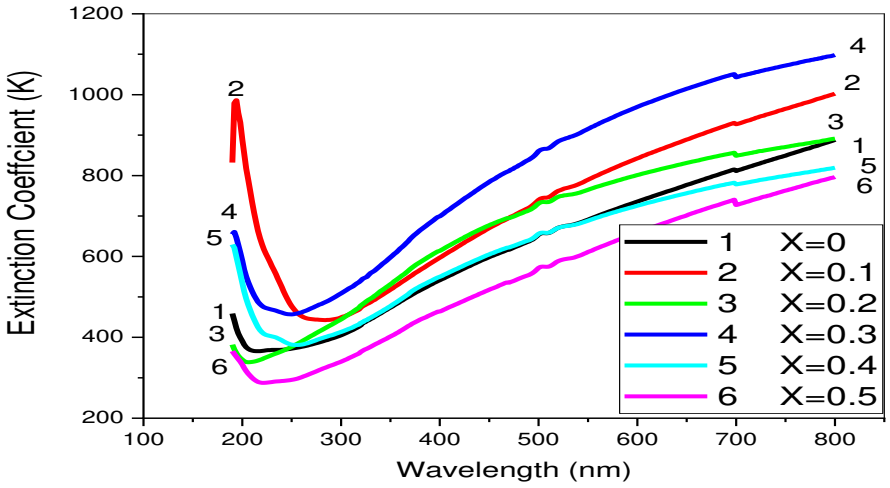


Figure 4 . Extinction coefficient (k) versus wavelength of $Zn_{1+x}Mn_xFe_{2-2x}O_4$ (X = 0.0, 0.1, 0.2, 0.3, 0.4 and 0.5) Nano composites

The refractive index show a decrease 1.563 to 2.948 ev and after that nearly from 4.5 to 6.5 ev with photon energy and Mn ions concentration(1-3), as shown in Fig 5. and table 3. The effects of large ionic size and concentration may be responsible for the decrease. The same behavior was report by [44] .

The dielectric function is directly associated with the energy band gap, and therefore, the dielectric constant during this work was obtund using the formula reported by. $\varepsilon = n^2$

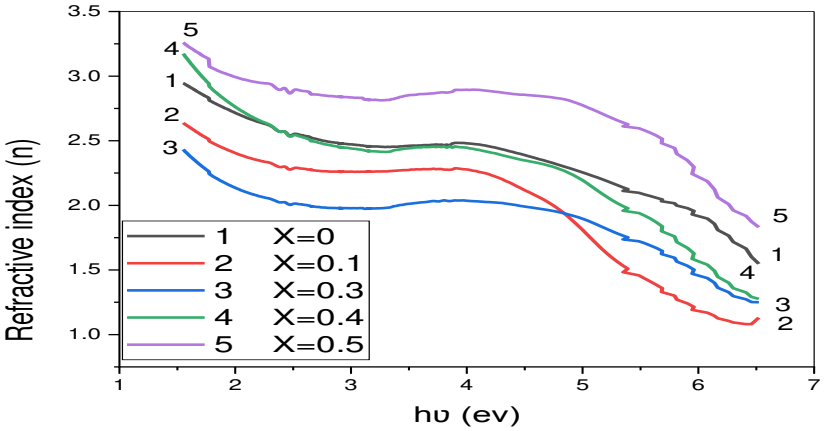


Figure 5. refractive index (n) of $Zn_{1+x}Mn_xFe_{2-2x}O_4$ Nano composites.

X	N	$\varepsilon=n^2$	$\varepsilon_{opt}=n^2-1$
0	2.562589	6.56686	5.56686
0.1	2.257383	5.09578	4.09578
0.2	2.314207	5.35555	4.35555
0.3	2.056235	4.2281	3.2281
0.4	2.570328	6.60609	5.60659
0.5	2.908934	8.4619	7.4619

Table 3. Refractive index (n), dielectric constant (ε), and optical dielectric constant (ε_{opt}) of the $Zn_{1+x}Mn_xFe_{2-2x}O_4$ Nano composites .

Optical Conductivity.

The optical Conductivity is another important parameter required for the design of optoelectronic devices. The optical Conductivity was calculated from the optical absorption coefficient α using the following relationship [45] .

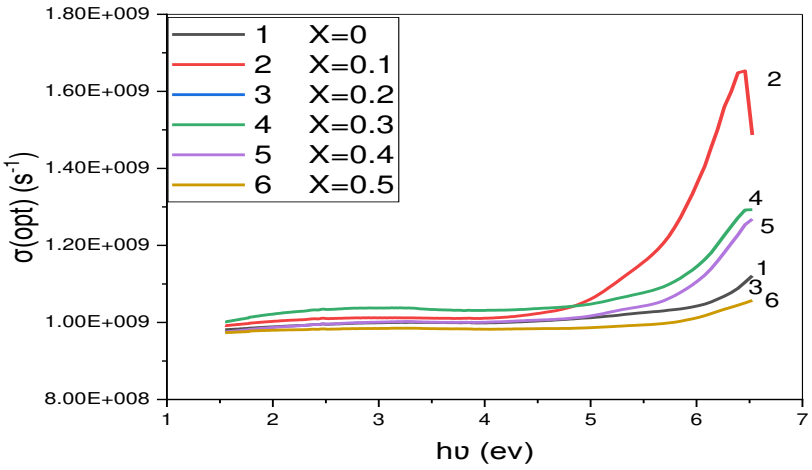


Figure 6. Optical Conductivity plots energy photon for $Zn_{1+x}Mn_xFe_{2-2x}O_4$ (X = 0.0, 0.1, 0.2, 0.3, 0.4, 0.5) Nano-composites .

Optical band gap energy :-

$$h\nu = A(h\nu - Eg)^n$$ [47]

Where A is the probability-dependent constant of the transition. eg denotes the optical band gap, hν is the photon energy, and n is a constant equal to 1/2 or 2 for a allowed direct or indirect transition, and 3 or 3/2 for a prohibited direct or indirect transition. Using Tauc plots $(\alpha h\nu)^2$ versus (hυ), the optical energy band gaps (Eg) were calculated. $(\alpha h\nu)^2$ versus (hυ) curves were plotted and shown in Figure 6 to evaluate the indirect band gap value of the resulting samples. The S-shaped profile of the $(\alpha h\nu)^2$ versus (hυ) curves indicates the presence of two distinct slopes and suggests that phonons play a role in the absorption process. Figure 6 shows the plots of the prepared samples , the indirect band gap energy value (Eg) was obtained by extrapolating a straight line at $(\alpha h\nu)^2 = 0$ for all fabricated samples.

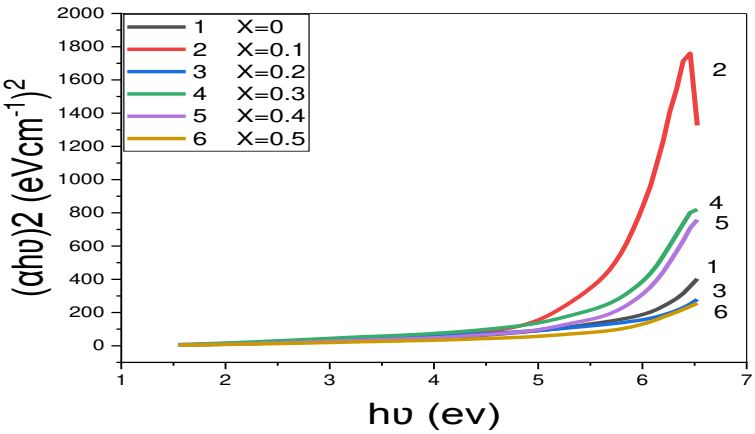
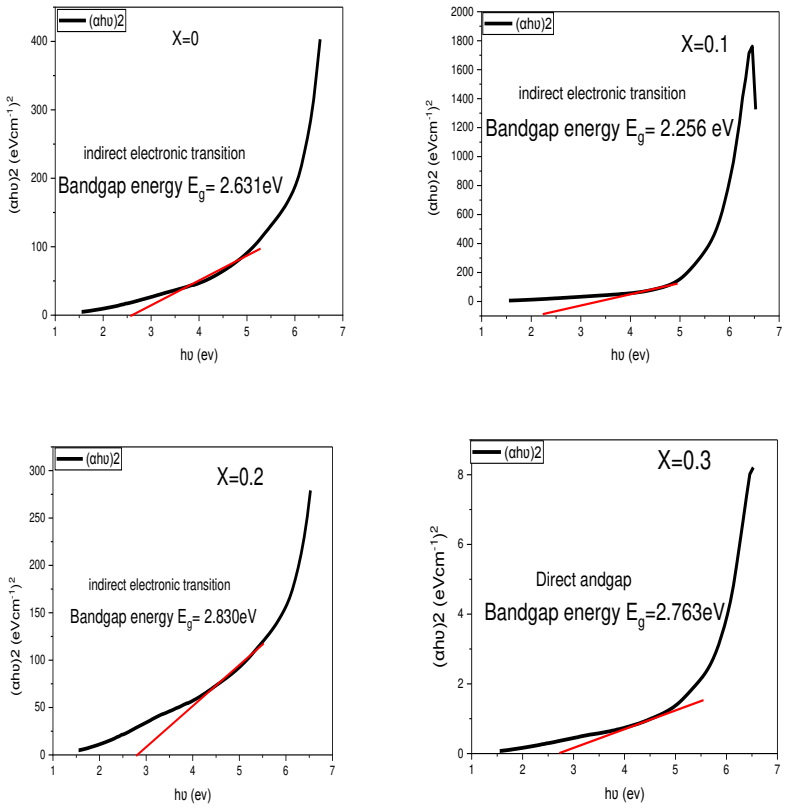


Figure 7. Optical band gap energy plots for $Zn_{1+x}Mn_xFe_{2-2x}O_4$ (X = 0.0, 0.1, 0.2, 0.3, 0.4, 0.5) nanocomposites



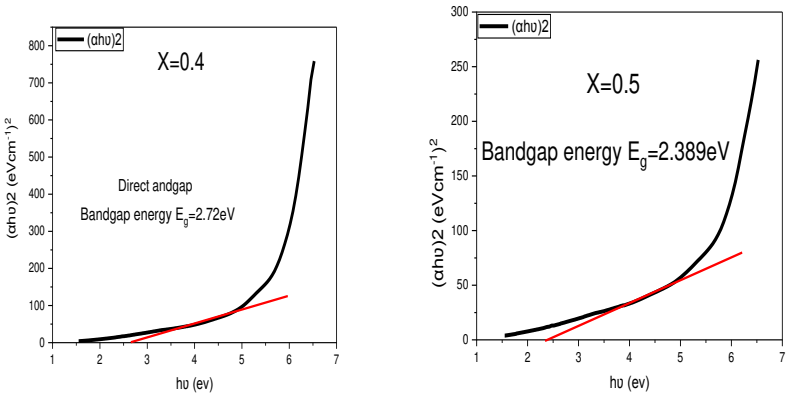


Figure 8. Optical band gap plots for $Zn_{1+x}Mn_xFe_{2-2x}O_4$ (X = 0.0, 0.1, 0.2, 0.3, 0.4, 0.5) (FMZ) Nano-composite.

Sample	X	Band gap (Ev)
Zn Fe_2O_4	0	2.631
$Zn_{1.1}Mn_{0.1}Fe_{1.8}O_4$	0.1	2.256
$Zn_{1.2}Mn_{0.2}Fe_{1.6}O_4$	0.2	2.830
$Zn_{1.3}Mn_{0.3}Fe_{1.4}O_4$	0.3	2.763
$Zn_{1.4}Mn_{0.4}Fe_{1.2}O_4$	0.4	2.720
$Zn_{1.5}Mn_{0.5}FeO_4$	0.5	2.389

Table 4. Optical band gap values of the $Zn_{1+x}Mn_xFe_{2-2x}O_4$ Nano-composites .

The optical energy band gap E_g values of $Zn_{1+x}Mn_xFe_{2-2x}O_4$ (X = 0.0, 0.1, 0.2, 0.3, 0.4 and 0.5) Nano particles for the direct electronic transition between the valence band V_{band} and conduction band C_{band} can be computed via Tauc's relation [33,46-47] As shown in Fig.7,8. The E_g values of $Zn_{1+x}Mn_xFe_{2-2x}O_4$ Nano-particles were calculated, which vary between 2.256eV and 2.830eV. However $Zn_{1+x}Mn_xFe_{2-2x}O_4$ displayed significant increased absorbance in the visible region due to incorporation of three metal oxide. The reason for the change in the band gap energy of the NCs compared to the individual metal oxides is likely due to the formation of new energy states at the interfaces between the different metal .

This can result in a shift in the electronic structure and a change in the band gap energy. Additionally, the presence of multiple metal oxides in the NCs can also lead to increased electron–hole separation and improved charge transport properties, which can further affect the band gap energy. This result was in good agreement with the literature [46] . which showed the possibility of using the prepared materials in some optical application .

AC electrical conductivity:-

Frequency dependence of a.c. conductivity.

The variation of electrical conductivity (σ_{ac}) of the $Zn_{1+x}Mn_xFe_{2-2x}O_4$ (x= 0.0, 0.1, 0.2, 0.3, 0.4 and 0.5) was performed at different temperatures with frequency was displayed, in figure 9 shows the variation of frequency-dependent AC conductivity of ferrites at different temperatures. The AC conductivity of all the samples is found to increase with increasing frequency and temperature, as has been observed. The hopping of charge carriers also increases with increasing frequency of the applied field, which increases conductivity. According to Koop's phenomenological theory [48] , which assumes that samples act as a multilayer capacitor, the increased AC conductivity with frequency and temperature is caused by the interfacial polarization. According to this hypothesis, the conductivity is caused by grain boundaries at low frequencies, but the dispersion is caused by the conducting grains at higher frequencies. Further, the Maxwell-Wagner two layers model is corresponded to the phenomenological theory [49, 50]

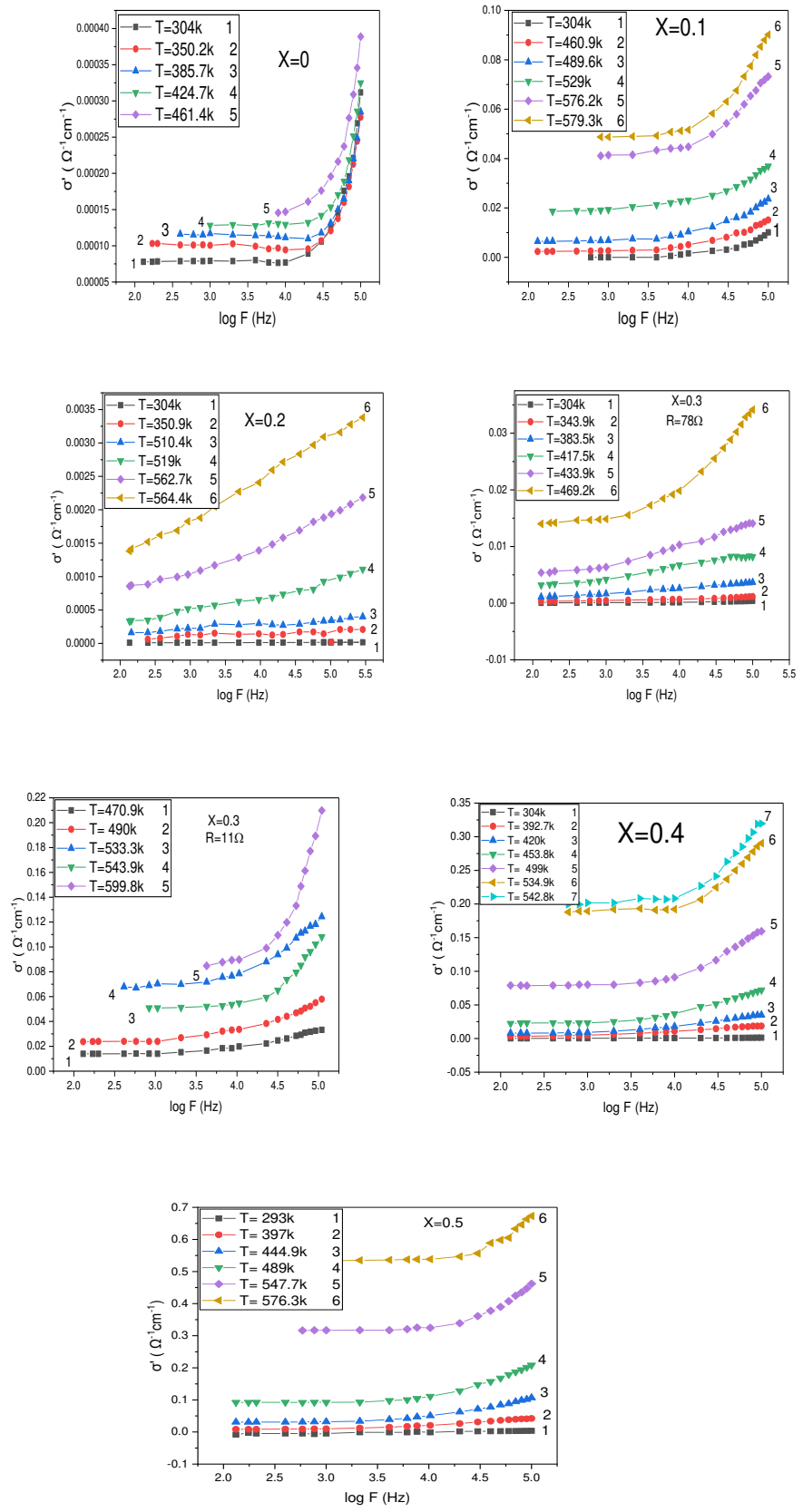
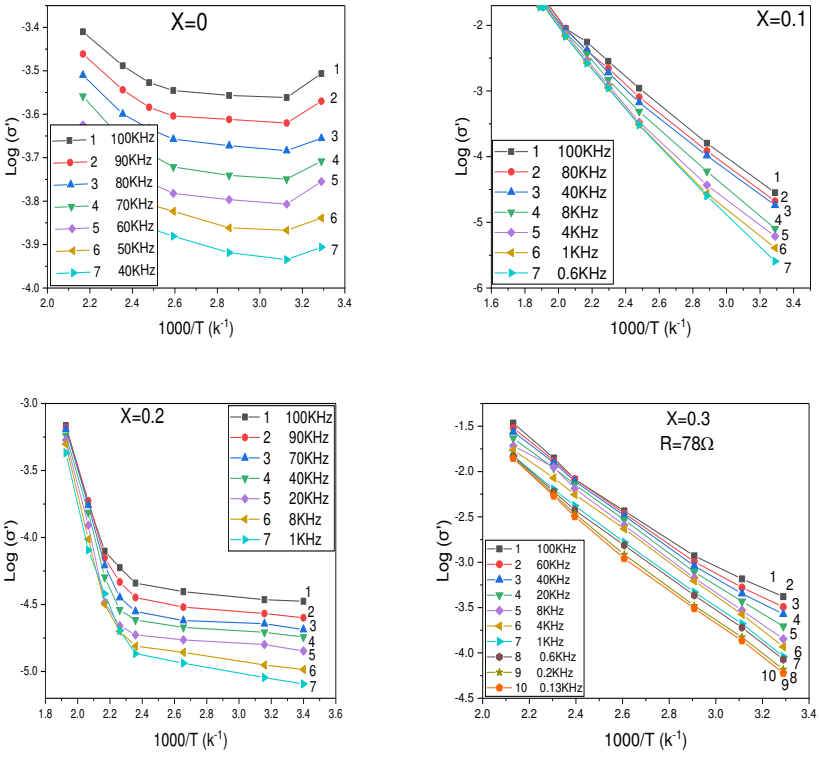


Fig. 9 Conductivity dependence of ac. frequency for all samples.

The dispersion has been observed in ac conductivity with temperature, demonstrating that conduction is a thermally induced process. At lower frequencies, the grain boundaries are more active; hence the hopping frequency of electrons between Fe^{3+} and Fe^{2+} ions is less. At high frequencies, ac conductivity curves are approaching each other, indicating the existence of various relaxation and thermally induced processes in the sample; therefore, the conductive grains become more active by promoting the hopping of electrons between Fe^{3+} and Fe^{2+} ions, increasing the hopping frequency. So, we observe the increase in conductivity with the increase in frequency. The figure shows an increase linearly with frequency and increases with temperature; additionally, the frequency dispersion of σ_{ac} in most cases has been observed. The results agree well with the theoretical relation between σ and ω ;

$$\sigma_{ac} = A(T)\ \omega^{S(T)} \quad 51,52$$

where *A* and *s* are parameters dependent on temperature, ω is the angular frequency and s is the frequency exponent.



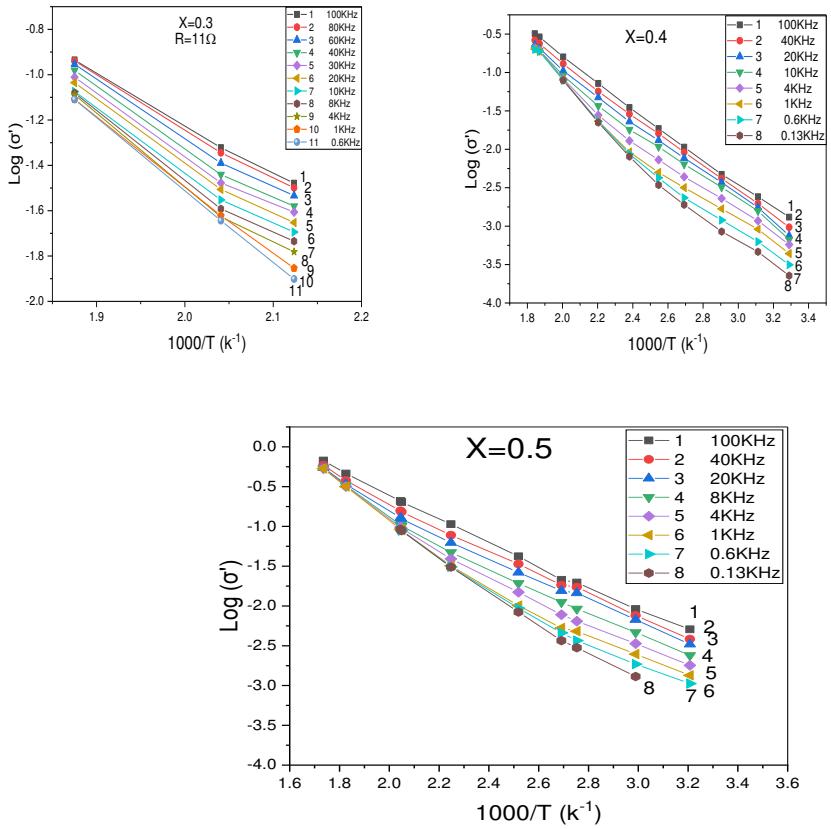


Fig. 10 Temperature dependence of a.c. conductivity. $Zn_{1+x}Mn_xFe_{2-2x}O_4$ (X = 0.0, 0.1, 0.2, 0.3, 0.4, 0.5) at different temperatures .

Temperature dependence of D.C. conductivity.

The DC electrical conductivity of zinc-manganese spinel ferrite was measured at different concentrations of zinc and manganese ions as a function of temperature. The log σ_{dc} on the inverse of temperature (1000/T) for structures where x is between 0.0 and 0.5. As shown in Figure 8, all samples exhibit semiconducting properties: σ_{dc} increases with temperature due to thermally activated charge carrier transfer to and from the Fe^{2+} and Fe^{3+} ions, consistent with the conduction mechanisms documented in substituted zinc-manganese ferrites . [53-54] . Direct current (DC) conductivity .The DC conductivity was calculated using the relationship

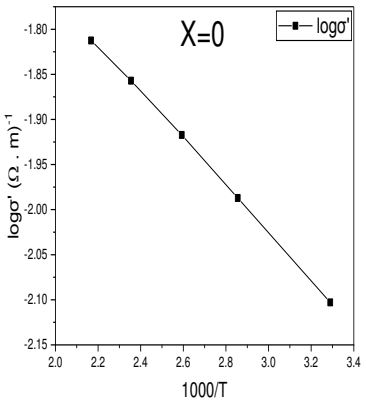
$$\sigma_{dc} = L/RA \quad [54]$$

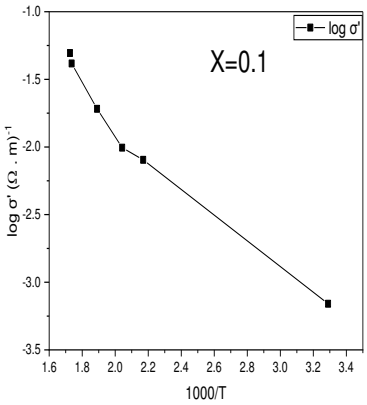
where L is the thickness of the sample, A is the cross-sectional area, and R is the measured resistance . The studied compound exhibits semiconducting behavior where charge transfer occurs primarily via electron hopping between polyvalent ions located at crystal sites, such as Mn^{3+}/Mn^{4+} and Fe^{2+}/Fe^{3+}. The probability of hopping increases with increasing temperature due to the increased thermal energy available to the electrons, leading to increased electrical conductivity . It was observed that the electrical conductivity increases with increasing temperature, indicating the semiconducting nature of the compound. The conductivity followed the Arrhenius equation

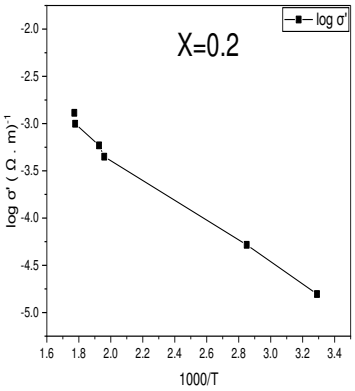
$$\sigma_{dc} = \sigma_0 \exp^{\frac{E}{K_B T}} \quad 54$$

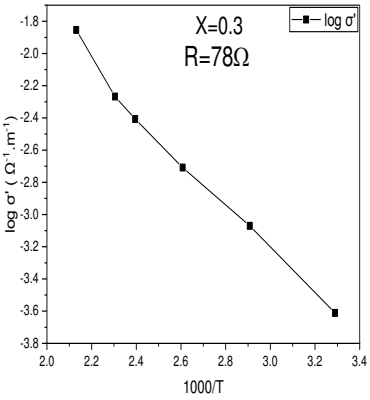
E is the activation energy ($E=E_a=E_g$), K_B is the Boltzmann constant and T is the temperature

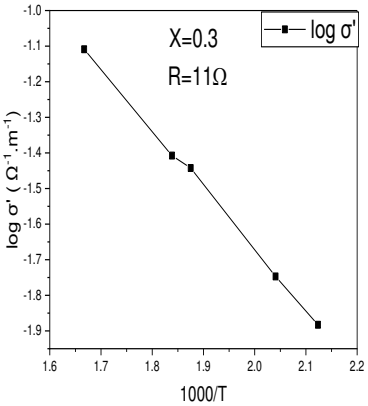
By plotting the relationship between Log σ_{dc} and 1000/T as shown in Fig 11., straight lines were obtained. The slope provides activation energy E, the Y- intercept reveals electrical conductivity (0. That's mean, confirming that the electron-hopping mechanism is the dominant mechanism .

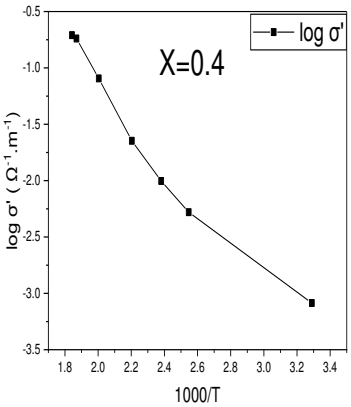

X=0
logσ'
logσ' (Ω . m)-1
1000/T


X=0.1
log σ'
log σ' (Ω . m)-1
1000/T


X=0.2
log σ'
log σ' (Ω . m)-1
1000/T


X=0.3
R=78Ω
log σ'
log σ' (Ω-1.m-1)
1000/T


X=0.3
R=11Ω
log σ'
log σ' (Ω-1.m-1)
1000/T


X=0.4
log σ'
log σ' (Ω-1.m-1)
1000/T

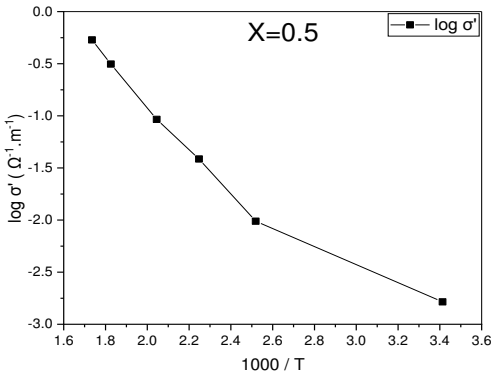


Fig. 11 Temperature dependence of DC conductivity for $Zn_{1+x}Mn_xFe_{2-2x}O_4$ Nano-composites

Activation energy (Ea) :-

X	Ea Ev
0	2.1865
0.1	2.1621
0.2	2.1462
0.3	2.0695
0.4	2.0853
0.5	2.2183

Table 4 Electrical activation energy (Ea) of the composite $Zn_{1+x}Mn_xFe_{2-2x}O_4$

This phenomenon is consistent with the Correlation Barrier Hopping CBH model, in which charge carriers hop over lower energy barriers at high frequencies.[55,56,57,58]

Conclusion

$Zn_{1+x}Mn_xFe_{2-2x}O_4$ doped with zinc (Zn^{2+}) and manganese (Mn^{4+}) ions was successfully prepared using the gel-solution auto-combustion method. X-ray diffraction (XRD) patterns showed the presence of a single crystalline phase in the cubic spinel form in all samples. Increasing the concentration of zinc (Zn^{2+}) and manganese (Mn^{4+}) ions leads to varying in crystal size and lattice parameter, as zinc (Zn^{2+}) ions are larger than

manganese (Mn^{4+}) ions. The particles were well-crystalline and agglomerated, according to FTIR and UV-Vis analysis XRD energy analysis revealed peaks for iron (Fe), manganese (Mn), zinc (Zn), and oxygen (O) present in all selected samples in precise manganese-to-zinc ratios. In the spinel structure, formed by the movement of A-site ions, oxygen ions, and B-site ions, the nanostructures exhibit a high diffuse reflection ratio, which increases with the addition of zinc (Zn^{2+}) ions. The observed fluctuation in electrical conductivity can be attributed to the significant electron transfer between iron(II) (Fe^{2+}) and iron(III) (Fe^{3+}) ions in determining the direction of electrical conductivity. The production of Fe^{2+} ions at octahedral sites leads to increased electron exchange between Fe^{2+}/Fe^{3+}, resulting in higher polarization and conductivity. These results indicate that all samples, with their high zinc and manganese content, high capacitance, and low loss, are suitable for use in capacitors for electronic devices such as computers, memory cards, and microwave absorbers.

Informed consent

Not applicable.

Declaration

The authors confirm that, the article is original, with the exceptions of those clearly identified in the text and supported by citations. The authors have quoted on the published work of others. All sources used on this work were correctly referenced and cited. This work has not previously served as a bases for, or been submitted for the award of any other. The datasets used and analyzed during the current study are available from the corresponding author on reasonable request.

Availability of Data and Materials

The datasets used and analysed during the current study are available from the corresponding author on reasonable request. All data generated or analysed during this study are included in this published article.

Data Availability

All data generated or analyzed during this study are included in this article, and any additional data will be made available upon request from the corresponding author (John Smith).

Funding.

No funding.

Author Contributions

(Abdul Hakim .A. Al-Hammadi , Fatima .A. Abuholikah , Fatima .M. Thabit) . Fatima .A. Abuholikah: Original draft, conceptualization, methodology, software, data collection, verification, and editing . Abdul Hakim .A. Al-Hammadi : Supervision, conceptualization, data collection, verification, and editing. Fatima .M. Thabit: Verification, review, and editing.

Additional Information

Please address correspondence and material requests to F. A. Abuholikah.

Reprint and licensing information is available at www.nature.com/reprints.

Publisher's Note: Springer Nature maintains neutrality regarding legal claims in published maps and institutional affiliations.

Open Access: This article is licensed under the Creative Commons Attribution 4.0 International License, which allows

use, sharing, modification, distribution, and reproduction in any medium or form, provided that the original author(s) and source are acknowledged, a link to the Creative Commons license is provided, and any changes are clearly indicated. Images or other third-party materials in this article are included under the article's Creative Commons license unless otherwise stated in the material's copyright information. If the material is not covered under the article's Creative Commons license, and your intended use is not permitted by law or exceeds permitted use, you will need to obtain direct permission from the copyright holder. To view a copy of this license, please visit the following link: http://creativecommons.org/licenses/by/4.0/.

© Author(s) 2026

References

1. Jadhav, P. A., Devan, R. S., Kolekar, Y. D. & Chougule, B. K. Structural, electrical and magnetic characterizations of Ni–Cu–Zn ferrite synthesized by citrate precursor method. *J. Phys. Chem. Solids* **70**, 396–400 (2009).

2. Gabal, M. A. Effect of Mg substitution on the magnetic properties of NiCuZn ferrite nanoparticles prepared through a novel method using egg white. *J. Magn. Magn. Mater.* **321**, 3144–3148 (2009).

3. Vadivel, M., Babu, R. R., Sethuraman, K., Ramamurthi, K. & Arivanandhan, M. Synthesis, structural, dielectric, magnetic and optical properties of Cr substituted CoFe2O4 nanoparticles by co-precipitation method. *J. Magn. Magn. Mater.* **362**, 122–129 (2014).

4. Khan, U. *et al.* Room and low-temperature magnetic characterization of Cr doped CoFe2O4 nanostructures. *Solid State Sci.* **133**, 107001 (2022).

5. Sabale, S., Khot, V., Jadhav, V., Zhu, X. & Xu, Y. Synthesis and properties of monodisperse superparamagnetic Mg0. 8Mn0. 2Fe2O4 nanoparticles using polyol reflux method. *Acta Metall. Sin. (English*

Lett. **27**, 1122–1126 (2014).

6. Ren, P., Zhang, J. & Deng, H. Preparation and microstructure of spinel zinc ferrite ZnFe2O4 by Co-precipitation method. *J. Wuhan Univ. Technol. Sci. Ed.* **24**, 927–930 (2009).

7. Gaikwad, P., Zimur, S., Sabale, S. & Kamble, P. Co2+ substituted ZnCuFe2O4 ($0.0 \leq x \leq 0.5$) ferrites: synthesis, magneto-structural and optical properties for their photocatalytic performance. *J. Supercond. Nov. Magn.* **32**, 2551–2558 (2019).

8. Jamil, M. T. *et al.* Effect on structural and optical properties of Zn-substituted cobalt ferrite CoFe2O4. *J. Ovonic Res.* **13**, 45–53 (2017).

9. Hammad, T. M., Salem, J. K., Amsha, A. A. & Hejazy, N. K. Optical and magnetic characterizations of zinc substituted copper ferrite synthesized by a co-precipitation chemical method. *J. Alloys Compd.* **741**, 123–130 (2018).

10. Sharifi, I., Shokrollahi, H. & Amiri, S. Ferrite-based magnetic nanofluids used in hyperthermia applications. *J. Magn. Magn. Mater.* **324**, 903–915 (2012).

11. Duong, B., Seraphin, S., Laokul, P., Masingboon, C. & Maensiri, S. Ni-Cu-Zn ferrite prepared by Aloe vera plant extract or egg white. *Microsc. Microanal.* **14**, 326–327 (2008).

12. Synthesis, L. E. Synthesis, properties, and applications of spinel cobalt ferritesCaldeira,. in *Environmental Applications of Nanomaterials* 1–16 (Springer, 2021).

13. Dhiman, P., Jasrotia, R., Goyal, D. & Mola, G. T. Hexagonal ferrites, synthesis, properties and their applications. *Mater. Res. Found* **112**, 336 (2021).

14. El Nahrawy, A. M., Abou Hammad, A. B. & Mansour, A. M. Compositional effects and optical properties of P2O5 doped magnesium silicate mesoporous thin films. *Arab. J. Sci. Eng.* **46**, 5893–5906 (2021).

15. Nirmala, T. S., Iyandurai, N., Yuvaraj, S. & Sundararajan, M. Third order nonlinear optical behavior and optical limiting properties of Ni2+

ions doped zinc nano-aluminates. *Opt. Mater. (Amst).* **124**, 111950 (2022).

16. You, J.-H., Kim, H.-J., Lee, J.-W. & Yoo, S.-I. Phase stability of SrZnxFe (2− x) Fe16O27 (0.0≤ x≤ 1.0) in low oxygen pressures. *Mater. Sci. Eng. B* **277**, 115563 (2022).

17. Nakamura, T. & Hatakeyama, K. Complex permeability of polycrystalline hexagonal ferrites. *IEEE Trans. Magn.* **36**, 3415–3417 (2002).

18. Rani, R. *et al.* Effect of zinc concentration on the magnetic properties of cobalt–zinc nanoferrite. *Ceram. Int.* **38**, 2389–2394 (2012).

19. Kakde, A. S. *et al.* Evidence of magnetic dilution due to unusual occupancy of zinc on B-site in NiFe2O4 spinel nano-ferrite. *J. Solid State Chem.* **300**, 122279 (2021).

20. Bera, P. *et al.* Solution combustion synthesis, characterization, magnetic, and dielectric properties of CoFe 2 O 4 and Co 0.5 M 0.5 Fe 2 O 4 (M= Mn, Ni, and Zn). *Phys. Chem. Chem. Phys.* **22**, 20087–20106 (2020).

21. Rana, G. *et al.* Recent advances on nickel nano-ferrite: A review on processing techniques, properties and diverse applications. *Chem. Eng. Res. Des.* **175**, 182–208 (2021).

22. Khodair, Z. T., Al-Saadi, T. M. & Abed, A. H. Effect of fuel on the structural and optical properties of MgO nanoparticles prepared by auto-combustion of sol–gel method. *Adv. Phys. Theor. Appl* **60**, (2016).

23. Hisham Alnahari, A.H. Al-Hammadi, Annas Al-Sharabi, Adnan Alnehia, The Effect of Tartaric Acid Concentration on the Structural, Morphological and Optical Properties of CuO–Fe2O3–MgO nanocomposites:Sana`a University Journal of Applied Sciences and Technology. Vol. 1(No. 2(page 78-87 (2023(

24. Cullity, B. D. *Elements of X-ray Diffraction*. (Hsin Yueh, 1986).

25. Monshi, A., Foroughi, M. R. & Monshi, M. R. World J. Nano Sci. Eng. (2012).

26. Bahramgour, M., Niaei, A., Asghari, E., Peighambardoust, S. J. &

Delibas, N. Enhancing structural and optical properties of hybrid perovskite layers with polymer modification. *Sci. Rep.* (2026).

27. Wiedemann, K. E. *et al.* Ibwder. Diffraction. *Powder Diffr.* **2**, (1987).

28. A.H. Al-Hammadi, Annas Al-Sharabi, Adnan Alnehia, Green and Chemically Prepared Zinc Sulfid Nanoparticles: A Comparative Study. :Sana`a University Journal of Applied Sciences and Technology. Vol. 1(No. 1(page 68-74 (2023(

29. Munawar, T., Iqbal, F., Yasmeen, S., Mahmood, K. & Hussain, A. Multi metal oxide NiO-CdO-ZnO nanocomposite–synthesis, structural, optical, electrical properties and enhanced sunlight driven photocatalytic activity. *Ceram. Int.* **46**, 2421–2437 (2020).

30. Al-Ariki, S. *et al.* Synthesis and comparative study on the structural and optical properties of ZnO doped with Ni and Ag nanopowders fabricated by sol gel technique. *Sci. Rep.* **11**, 11948 (2021).

31. Eman Mohammed Ali Nassar, A.H. Al-Hammadi and Yasser Hussein Issa Mohammed, Morphological and Optical Analysis of Al2O3 :Zn Nanoparticles:Sana`a University Journal of Applied Sciences and Technology. Vol.3 No. 3, page 1408- 1418, 2025.

32. Rajeh, A., Ragab, H. M. & Abutalib, M. M. Co doped ZnO reinforced PEMA/PMMA composite: structural, thermal, dielectric and electrical properties for electrochemical applications. *J. Mol. Struct.* **1217**, 128447 (2020).

33. Al-Sharabi, A., Alnehia, A., Al-Hammadi, A. H., Alhumaidha, K. A. & AL-Osta, A. The effect of Nigella sativa seed extract concentration on crystal structure, band gap and antibacterial activity of ZnS-NPs prepared by green route. *J. Mater. Sci. Mater. Electron.* **33**, 20812–20822 (2022).

34. Abutalib, M. M. & Rajeh, A. Enhanced structural, electrical, mechanical properties and antibacterial activity of Cs/PEO doped mixed nanoparticles (Ag/TiO2) for food packaging applications. *Polym. Test.* **93**, 107013 (2021).

35. Chukanov, N. V. *Infrared spectra of mineral species: Extended library*. (Springer Science & Business Media, 2013).

36. Islam, R., Hakim, M. A., Rahman, M. O., Das, H. N. & Mamun, M. A. Study of the structural, magnetic and electrical properties of Gd-substituted Mn–Zn mixed ferrites. *J. Alloys Compd.* **559**, 174–180 (2013).

37. Desai, K. R. *et al.* X-ray diffraction based Williamson–Hall analysis and rietveld refinement for strain mechanism in Mg–Mn co-substituted CdFe2O4 nanoparticles. *Phys. B Condens. Matter* **614**, 413054 (2021).

38. Abdel-Kader, S. R., El-Awad, A. M. & Abdel Rahim, M. A. Influence of calcination temperature on the properties and photocatalytic efficiencies of BiFe0. 9Cu0. 1O3 nanoparticles. *Sci. Rep.* (2026).

39. Al-Hammadi, A. H., Othman, A. A. M. & Khoreem, S. H. Influence of manganese doping on optical properties of barium ferrites nanoparticles. *Bioint Res Appl Chem* **13**, 369 (2022).

40. Alnehia, A., Al-Hammadi, A. H., Al-Sharabi, A. & Alnahari, H. Optical, structural and morphological properties of ZnO and Fe+ 3 doped ZnO-NPs prepared by Foeniculum vulgare extract as capping agent for optoelectronic applications. *Inorg. Chem. Commun.* **143**, 109699 (2022).

41. Ahmed, A.-O., Alnehia, A., Qaid, A. A., Al-Ahsab, H. T. & Al-Sharabi, A. Structural, morphological and optical properties of Cr doped ZnS nanoparticles prepared without any capping agent. *Optik (Stuttg).* **214**, 164831 (2020).

42. Asma`a Ahmed Al-Adhrreai, A.M. Abdulwahab and A.H. Al-Hammadi Structural, Optical and Cytotoxic Analysis of Sr-Doped CuS Nanoparticles for Lung Cuncer Applcation. *Sana`a University Journal of Applied Sciences and Technology.3(4) (2025). 990-998.*

43. Onochie, U. P. *et al.* Analysis of optical band gap and urbach tail of zinc sulphide coated with aqueous and organic dye extracts prepared by chemical bath deposition technique. *Opt. Mater. (Amst).* **114**, 110970 (2021).

44. Bagade, A. *et al.* Impact of Mg2+ substitution on structural, magnetic

and optical properties of Cu-Cd ferrites. *Mater. Today Proc.* **53**, 144–152 (2022).

45. Nadeem, M. S. *et al.* Hydrothermally derived co, Ni co-doped ZnO nanorods; structural, optical, and morphological study. *Opt. Mater. (Amst).* **111**, 110606 (2021).

46. Rahman, A. et al. Structural, optical and photocatalytic studies of trimetallic oxides nanostructures prepared via wet chemical approach. Synth. Met. 259, 116228 (2020). *Optik (Stuttg).* **260**, 169124 (2022).

47. Mukhtar, F. *et al.* Dual S-scheme heterojunction ZnO–V2O5–WO3 nanocomposite with enhanced photocatalytic and antimicrobial activity. *Mater. Chem. Phys.* **263**, 124372 (2021).

48. Raddaoui, Z. *et al.* Hopping conduction mechanism and impedance spectroscopy analyses of La0. 70Sr0. 25Na0. 05Mn0. 70Ti0. 30O3 ceramic. *J. Mater. Sci. Mater. Electron.* **32**, 16113–16125 (2021).

49. Koops, C. G. On the dispersion of resistivity and dielectric constant of some semiconductors at audiofrequencies. *Phys. Rev.* **83**, 121 (1951).

50. Kurien, S., Mathew, J., Sebastian, S., Potty, S. N. & George, K. C. Dielectric behavior and ac electrical conductivity of nanocrystalline nickel aluminate. *Mater. Chem. Phys.* **98**, 470–476 (2006).

51. Assim, E. M. & El-Metwally, E. G. A study on electrical (dc/ac) conductivity and dielectric characteristics of quaternary Ge50In4Ga13Se33 chalcogenide thin films. *J. Non. Cryst. Solids* **566**, 120892 (2021).

52. El Ata, A. M. A., El Nimr, M. K., Attia, S. M., El Kony, D. & Al-Hammadi, A. H. Studies of AC electrical conductivity and initial magnetic permeability of rare-earth-substituted Li–Co ferrites. *J. Magn. Magn. Mater.* **297**, 33–43 (2006).

53. Ahmed, M. A., Okasha, N. & Kershi, R. M. Dramatic effect of rare earth ion on the electrical and magnetic properties of W-type barium hexaferrites. *Phys. B Condens. Matter* **405**, 3223–3233 (2010).

54. Varshney, D., Verma, K. & Kumar, A. Substitutional effect on structural

and magnetic properties of AxCo1− xFe2O4 (A= Zn, Mg and x= 0.0, 0.5) ferrites. *J. Mol. Struct.* **1006**, 447–452 (2011).

55. Koseoğlu, Y.: Structural, magnetic. Electrical conduction and magnetoelectric effect in Ni0. 50 Co0. 50 Fe2O4+ Ba0. 8 Pb0. 2TiO3 composites. *Mater. Res. Bull.* **39**, 2265–2272 (2004).

56. Köseoğlu, Y. Structural, magnetic, electrical and dielectric properties of MnxNi1− xFe2O4 spinel nanoferrites prepared by PEG assisted hydrothermal method. *Ceram. Int.* **39**, 4221–4230 (2013).

57. Addayeva, Z., Muradov, M., Eyvazova, G., Niftiyev, N. & Mammadov, F. Effect of temperature and AC field duration on the dielectric behavior of PVA/GO/FeGaInS 4 nanocomposites. *RSC Adv.* **15**, 49307–49319 (2025).

58. Desmond, M., Mavrogiannis, N. & Gagnon, Z. Maxwell-Wagner Polarization and Frequency-Dependent Injection<? format?> at Aqueous Electrical Interfaces. *Phys. Rev. Lett.* **109**, 187602 (2012).